Electrochimica Acta 76 (2012) 487–494

Contents lists available at SciVerse ScienceDirect

Electrochimica Acta

journal homepage: www.elsevier.com/locate/electacta

Boron doped nanocrystalline diamond microelectrodes for the detection of Zn^{2+} and dissolved O_2

E.L. Silva*, A.C. Bastos, M.A. Neto, R.F. Silva, M.L. Zheludkevich, M.G.S. Ferreira, F.J. Oliveira

CICECO – Department of Ceramics & Glass Engineering, University of Aveiro, Campus Universitário de Santiago, 3810-193 Aveiro, Portugal

ARTICLE INFO

Article history:
Received 15 December 2011
Received in revised form 22 May 2012
Accepted 22 May 2012
Available online 30 May 2012

Keywords:
B-NCD
Microelectrodes
Zinc
Corrosion
Amperometric

ABSTRACT

Boron-doped nanocrystalline diamond (B-NCD) films were grown by the hot filament chemical vapor deposition (HFCVD) technique on top of sharp electropolished tungsten substrates, in order to create amperometric microelectrodes (MEs) for detection of Zn^{2+}(aq) and dissolved O_2. The boron source was a B_2O_3 + ethanol mixture dragged by Argon gas through a bubbler. Different B_2O_3 concentrations were used to study the doping effect on the electrochemical behavior. The B-NCD MEs exhibited a working potential window of about 3.5 V in 5 mM NaCl, with low background current and good chemical inertness. The best electrochemical kinetics was achieved for the ME with highest boron doping content. The linear relationship between zinc concentration and zinc reduction current was found in a wide concentration interval from 10^{-5} M to 10^{-2} M of $ZnCl_2$ in a 5 mM NaCl background. Measurements with a Fe–Zn galvanic couple immersed in 5 mM NaCl demonstrate potential applicability of the B-NCD ME for use in localized corrosion studies.

1. Introduction

Apart from its outstanding mechanical and thermal properties [1], CVD diamond has been object of intense study for the last two decades due to its promising electrical properties, when doped by other elements, particularly boron [2–4]. Therefore diamond was studied for electrochemical purposes [5] taking into account its superior chemical stability. Boron-doped CVD diamond was reported to exhibit a potential window of water stability wider than any other solid electrode material. A very low background current and extreme chemical inertness and resistance to fouling due to the non-polar H terminated surface can also be counted as important advantages [6–8]. The promising results have encouraged high interest on diamond to be applied for microelectrodes as well [9]. As a result of electrode miniaturization to a critical dimension of <25 μm [10], which enables working with enhanced mass transport and steady state currents, as well as measurements in high resistivity media, CVD diamond microelectrodes (MEs) became an increasing matter of research, mainly in the biological field.

A variety of microstructures ranging from microcrystalline to nanocrystalline diamond can be obtained by synthesis in metastable conditions, which is the case of CVD methods such as the hot filament assisted CVD (HFCVD). Nanocrystalline diamond is the most interesting for MEs because of its grain size allowing maximum miniaturization of the electrode [11]. Although there are many bio-related publications with diamond electrodes [12–17] and some works concerning the detection of trace metals and use of B-doped diamond electrodes in SECM [18–20], to our knowledge there are no published works applying B-doped diamond MEs to the corrosion field, where they can also play an important role.

Our main interest in this work was focused on optimization of the electrochemical properties of boron-doped nanocrystalline diamond (B-NCD) films to be used in amperometric MEs for corrosion studies. An example of such measurement is the distribution mapping of electrochemically active species generated or consumed in confined areas on corroding metal surface. Such experiments are of prime importance for understanding mechanisms and kinetics of corrosion and self-healing processes in the local defects of active coatings [21,22]. Particular interest is in the case of metal cations that are reduced at potential range where the reduction of water and dissolved oxygen can mask their amperometric detection. This is a limiting condition for most electrode materials currently in use but it may be an opportunity for B-NCD based MEs. One of the most corrosion relevant cases is determination of local concentration of zinc cations in the electrolytes near corroding surface of galvanized steel. Zinc has widespread applications of great importance such as galvanic coatings on steel, as anodes for common batteries or in brass metallurgy. It is also relevant in the metabolism of plants, animals and microorganisms [23–25].

The quantification of zinc is therefore a significant matter for many different areas, but the means available are limited mostly to spectroscopic and electrochemical stripping techniques [26–28].

* Corresponding author. Tel.: +351 234 370354; fax: +351 234 370204.
E-mail address: elsilva@ua.pt (E.L. Silva).

0013-4686/$ – see front matter © 2012 Elsevier Ltd. All rights reserved.
http://dx.doi.org/10.1016/j.electacta.2012.05.074

Recently, Strasunske et al. [29] obtained good results by using silver amalgam electrodes (3 mm in diameter) to analyze river water by differential pulse anodic stripping voltammetry. Tada et al. has reported the voltammetric detection of Zn^{2+} by using a small zinc disk electrode to probe the corrosion of Zn/steel couple, but within a narrow concentration range and with millimetric, not micrometric, resolution [30]. Attempts also have been made for localized potentiometric detection of Zn^{2+} with ion-selective microelectrodes but the electrodes still present low sensitivity, low selectivity, short lifetime and complex fabrication [31,32]. In terms of the use of B-NCD electrodes, the group of Swain has reported satisfactory results using B-NCD electrodes for the detection of Zn^{2+} and other heavy metals by anodic stripping voltammetry, although large metal deposits and electrode fouling were a problem [33,34]. However, the size of the electrode again does not allow the spatial mapping in the micrometric range.

In the present work, we report the fabrication of B-NCD microelectrodes and their use as probes for Zn^{2+} and oxygen detection by performing cyclic voltammetry (CV) and microamperometry measurements at fixed potential in zinc chloride solutions and in a model Zn–Fe galvanic corrosion system.

2. Experimental

2.1. Microelectrode fabrication

2.1.1. Substrate preparation

Electroposharpened tungsten wires (99.9%+, 125 μm, Goodfellow, England) were used as a body of electrode. The sharpening of the wires was performed via electropolishing in a custom-made dynamic flow system, using a 3 M NaOH solution. Each filament was connected as a working electrode (anode) in the electropolishing system and was sharpened by applying a potential difference of 10 V between the working and the counter electrode during 50 s while keeping the solution flowing. The tips were sharpened down to radii of <100 nm and ultrasonically cleaned with distilled water. Afterwards they were ultrasonically seeded during 10 min in a suspension of nanodiamond powder (~6 nm, 98+%, ABCR, Germany) in distilled water and ultrasonically cleaned during 15 min in ethanol to remove the rest of powder.

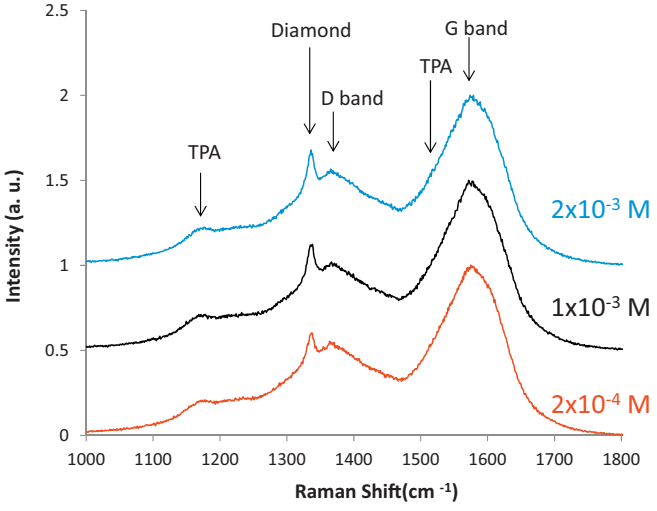

Fig. 1. Raman spectra (325 nm wavelength) of the B-NCD films grown with different B_2O_3 concentrations of 2×10^{-4}, 1×10^{-3} and 2×10^{-3} M. There are five main features: at 1140 and 1470 cm^{-1}, assigned to transpolyacetylene (TPA) in the grain boundaries; at 1333 cm^{-1}, indicating the presence of diamond crystals; at 1340 cm^{-1} and 1540 cm^{-1}, assigned to the D and G bands of graphite, respectively.

2.1.2. Diamond film growth

The diamond films were grown by HFCVD with four tungsten filaments at a temperature of 2300 °C that worked as gas activators and substrate heating sources. The sharpened tungsten tips were positioned horizontally on a substrate holder below the filaments at a distance of 7 mm. B-NCD films were grown during 30 min. The substrate temperature and the total gas pressure were kept constant at 770 °C and 180 mbar, respectively. The gas phase was composed by hydrogen and methane with a 0.07 CH_4/H_2 ratio with addition of the boron doping mixture. The boron source for doping the films was a solution of boron oxide (B_2O_3, 99.6%, ABCR) dissolved in ethanol inside a gas washing bottle. This boron-containing solution was dragged by argon gas into the CVD reaction chamber, with a constant $(Ar + B)/H_2$ ratio of 0.03. Solutions with three different B_2O_3 concentrations of 2×10^{-4}, 1×10^{-3} and 2×10^{-3} M were tested for the S1, S2 and S3 microelectrodes, respectively. The microstructure of the grown films was evaluated by scanning electron microscopy (Hitachi SU-4100). UV μ-Raman spectroscopy (HORIBA JOBIN YVON HR800UV), using the line 325 nm from a He–Cd laser (KIMMON IK series) for surface excitation, allowed the identification of the different carbon sp^2/sp^3 phases incorporated in the coatings and the presence of residual stresses.

2.1.3. Electroactive area delimitation

The B-NCD covered tungsten wires were partially insulated with acid resistant varnish (Lacomit, AGAR) with the aid of a micrometric manipulator under a microscope in order to limit the electroactive area just at the apex.

2.2. Electrochemical measurements

2.2.1. Electrode characterization

The electrochemical response of the B-NCD MEs was tested by cyclic voltammetry with a AUTOLAB PGSTAT302N potentiostat/galvanostat (Eco Chemie, The Netherlands). The electrochemical cell was kept inside a Faraday cage, open to air, and consisted on the B-NCD ME as working electrode, a platinum counter-electrode and a saturated calomel electrode (SCE) as reference. All potentials in this paper are referred to SCE except for the line and 2D-map scans in corrosion testing, where a Ag/AgCl electrode was used as reference. The electron transfer kinetics was evaluated in 10 mM $Fe(CN)_6^{3-/4-}$ in 5 mM NaCl (all reagents were *pro analysis* grade from Riedel-deHäen). The B-NCD MEs were compared with platinum and gold microelectrodes (10 μm discs embedded in cylindrical glass with a conical tip of 200 μm in diameter) for the detection of Zn^{2+} in $ZnCl_2$ solutions ranging from 10^{-6} M to 10^{-2} M in 5 mM NaCl (pH = 2). All potentiodynamic measurements were performed with a scan rate of 100 mV s^{-1}.

2.2.2. Application to corrosion testing

A model system consisting of a Fe–Zn galvanic couple immersed in 5 mM NaCl solution was used in order to evaluate applicability of the B-NCD MEs for mapping the distribution of Zn^{2+} and O_2 near active corroding metallic surfaces. Microamperometry measurements were performed with an IPA2 amplifier (Applicable Electronics Inc., USA) in the voltammetric/amperometric mode, using a 2 electrode arrangement, with a Ag/AgCl electrode as counter and reference electrode. Linear or 2D scans were done using B-NCD ME at a distance of 100 μm from the surface. Lines and maps were recorded at a potential of −0.9 V (vs. Ag/AgCl) for detection of dissolved O_2 and −1.6 or −1.3 V (vs. Ag/AgCl) for detection of Zn^{2+}.

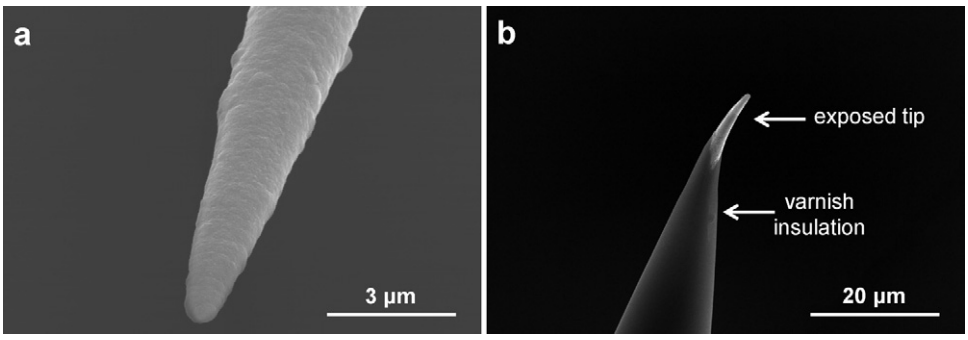

Fig. 2. SEM micrographs of (a) B-NCD film grown on top of sharp tungsten wire, (b) B-NCD probe insulated with varnish, showing a typical exposed area.

3. Results and discussion

3.1. Electrode characterization

The microscopic observations of the coated W-microelectrodes demonstrate presence of a dense intact diamond layer on the metal surface, which was confirmed by Raman spectroscopy. Each of the Raman spectra in Fig. 1 shows the following features: (i) at 1140 and 1470 cm^{-1}, commonly assigned to transpolyacetylene (TPA) in the grain boundaries; (ii) at 1333 cm^{-1}, indicating the presence of diamond crystals; (iii) at 1340 cm^{-1} and 1540 cm^{-1}, assigned to the D and G bands of graphite, respectively [35]. No voids are observed at the B-NCD films, meaning that the tungsten tip is well insulated from the analyte by the B-NCD coating (Fig. 2a). Good coverage and intactness of the diamond film is crucial in order to avoid the penetration of electrolyte to the metal surface and the consequent electrochemical response o tungsten during the measurements. The tungsten tips with B-NCD films were coated with a polymer layer in order to provide an electrical insulation leaving only an apex as exposed zone of the probe. The exposed area was about ~30 μm^2 with a tip radius of ~0.5 µm (Fig. 2b).

The CV measurements were performed on a bare tungsten microelectrode in the potential range from −1.5 to 1 V in 5 mM NaCl in order to exclude the situation of W-substrate contribution for the electrochemical measurements (Fig. 3a). Besides water reduction, three oxidation peaks are observed that can be related to the formation of W_2O_5, WO_2 and WO_3 at the tungsten surface, since these are known to be the most stable oxide products [36]. None of these peaks was observed in the current-potential curve of the B-NCD microelectrode as shown in Fig. 3a (inset) in the same solution within the referred potential range, confirming the absence of response from the W substrate. Instead, only water oxidation (starting at ~1 V) and a small response from water reduction were observed. The kinetics for the latter process is extremely slow at the B-NCD surface as can be seen in Fig. 3b for the S1 ME, which shows a very high overpotential for hydrogen evolution. This behavior corresponds to a ~3.5 V usable window, which is larger than the 2.5–3.0 V window reported in various works for B-NCD [37–39]. The response of the B-NCD MEs was also compared with platinum and gold MEs in the same solution. It can be observed that the reduction of dissolved oxygen and water are easier on both platinum and gold, with overpotentials lower than the exhibited by the B-NCD MEs, although they do present a higher overpotential for water oxidation.

The unfavorable kinetics for water and oxygen reduction at the B-NCD surface, however, could be also an indication of slow kinetics for other processes. For obvious reasons, there is no point in producing MEs with extensive potential windows if the electron transfer kinetic is not adequate within the working window. Attending to the electrochemical properties of CVD diamond and, in particular, to the microstructure of NCD, the slow kinetics of this material is likely to be associated with low conductivity originated by ineffective boron doping. NCD presents a huge number of grain boundaries due to the size of its crystallites. These regions can contain a high amount of different non-diamond carbon species such as graphitic phases and trans-polyacetylene which are sp^2 bonded when NCD is grown by HFCVD [35]. The grain boundaries can be a problem for the overall electrical conductivity of doped NCD films in several ways. First, although the non-diamond carbon phases in the boundaries can provide electrical conductivity to undoped NCD, they are not a reliable form of charge transport because of the implicit instability of these carbon forms, which can easily be etched or oxidized, either electrochemically or thermally [40]. Conversely, by promoting the substitutional incorporation of boron atoms into carbon lattice positions, electric conduction by electronic holes is enabled in a consistent manner, ensuring the reliability of the material's

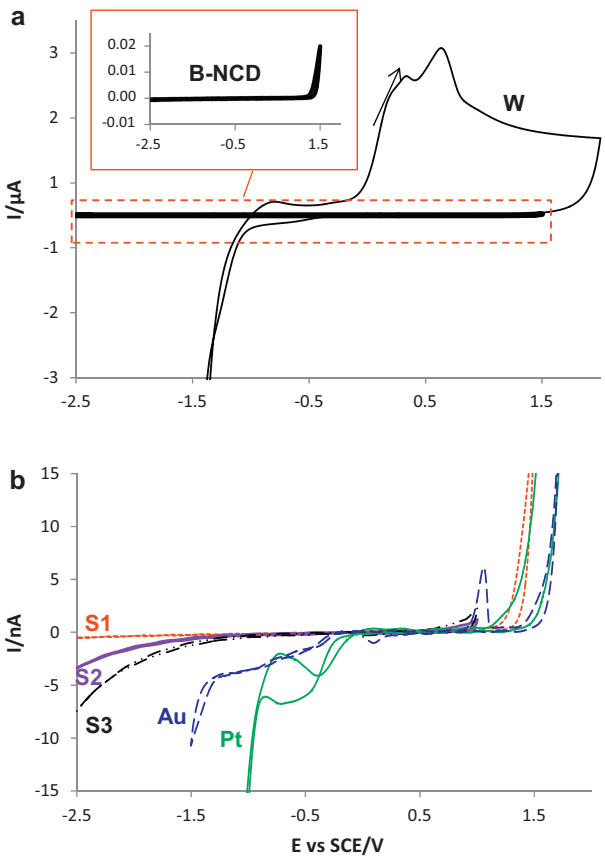

Fig. 3. Voltammograms of (a) a bare tungsten microelectrode and a B-NCD (S1) probe in 5 mM NaCl, (b) Pt, Au and S1, S2 and S3 B-NCD microelectrodes in 5 mM NaCl.

Table 1
Electrochemical kinetic parameters for three B-NCD MEs grown with different [B_2O_3] (ΔE_p, peak potential separation; i_{ox}, oxidation peak current; I_p^{ox}, ratio of oxidation peak currents, I_p^{red}, ratio of reduction peak currents).

Film	ΔE_p (mV)	I_p^{ox} (μA)	I_p^{ox}/I_p^{red}
S1	302	0.048	0.92
S2	222	0.105	1.17
S3	101	0.162	1.32

electrical conductivity and chemical stability. The second way is also related to sp^2 carbon π bonds and their unsaturated nature, which increase the reactivity of the B-NCD film and also ease the poisoning of the surface [41]. A third mechanism how grain boundaries affect the conductivity of the NCD films is by acting as "sinks" for the boron atoms, thereby reducing the doping degree. According to Goss et al., grain boundaries and near grain edge sites require lower energy for boron integration than intra-grain positions. However boron only contributes to the overall conductivity of the film by occupying substitutional positions in the diamond lattice [42]. Even though grain boundaries are a problem, reducing their number would contribute to a coarsening of the surface microstructure of the ME and could compromise the electrode miniaturization level. The solution relied on improving the conductivity of the MEs by increasing the boron content through higher B_2O_3 concentrations in the doping solutions. Fig. 3b shows that raising the boron concentration in the solution from 10^{-4} M for the S1 ME to 10^{-3} M for S2 and 2×10^{-3} for the S3 ME resulted in a slight narrowing of the working potential window but also contributed to an improvement in the electrode transfer kinetics, as is shown in the CV curves on Fig. 4 for the $Fe(CN)_6^{3-/4-}$ redox system. The peak separation, ΔE_p, decreased from 302 mV in S1 to 101 mV in S3, along with the increase of the current peak values (Table 1). Although the ΔE_p for reversible 1 electron reactions is expected to be around 59 mV [43], the ΔE_p variation from S1 to S3 indicates a more reversible behavior at the surface of the S3 ME.

An alternative to changing the amount of boron doping is varying the Ar + B flow, but this would also change the amount of

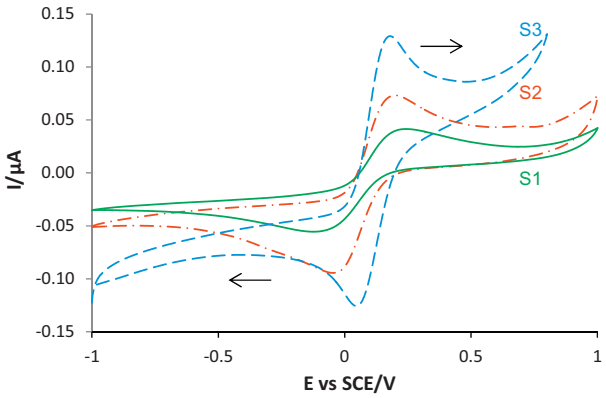

Fig. 4. Voltammograms using S1, S2 and S3 B-NCD microelectrodes in 10 mM $Fe(CN)_6^{3-/4-}$ + 5 mM NaCl.

available carbon in the active gas phase leading to the deposition of high amounts of sp^2 bonded non-diamond material in the B-NCD films. Thus a good compromise between fast kinetics and acceptable working potential window was obtained in the case of S3 ME particularly for negative potentials which is the region of interest for the detection of Zn^{2+}.

3.2. Zn^{2+} detection

Several MEs with the S3 composition were studied for the detection of Zn^{2+} and dissolved oxygen. The first step was to compare B-NCD MEs with common inert electrode materials such as platinum and gold. The detection of zinc was performed in acidified $ZnCl_2$ solutions (pH 2) since at this pH Zn^{2+} is clearly dominant over other soluble species such as $ZnCl^+$ and $ZnOH^+$. The formation of carbonated zinc species is also not favorable in acidic conditions [44,45]. Cyclic voltammetry was also performed on Pt and Au MEs in $ZnCl_2$ solutions with Zn^{2+} concentrations of 10^{-5}, 10^{-4} and 10^{-3} M in a 5 mM NaCl background. The results are presented in Fig. 5a–c, where the inability of these materials to accurately reduce Zn^{2+} to

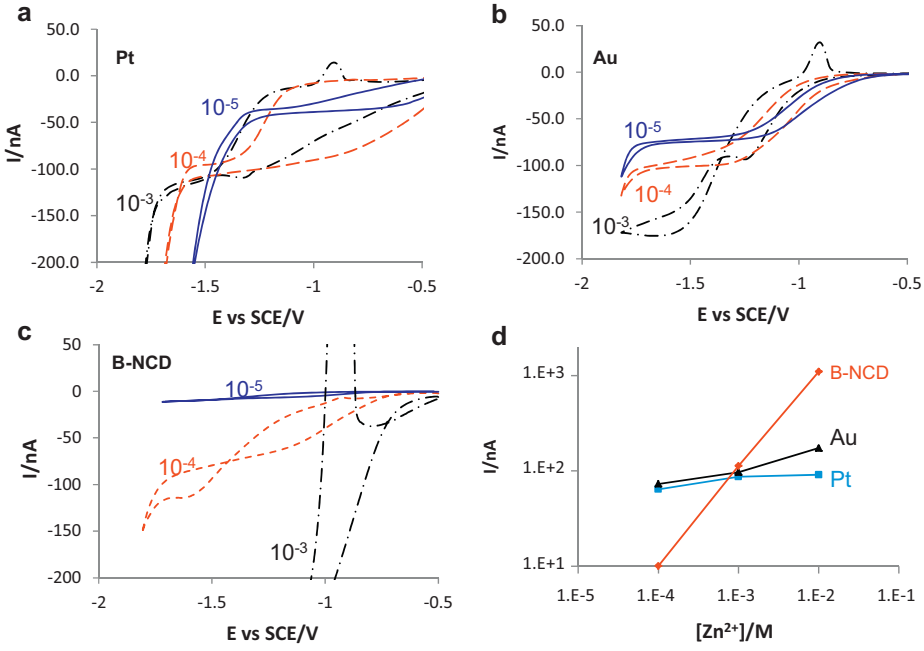

Fig. 5. Voltammograms using (a) Pt, (b) Au and (c) B-NCD microelectrodes in $ZnCl_2$ solutions of 10^{-5}, 10^{-4} and 10^{-3} M in 5 mM NaCl, revealing the good performance of B-NCD for the reduction of Zn^{2+} in comparison with the poor behavior exhibited by Pt and Au. (d) Current–concentration curves for B-NCD, Pt and Au microelectrodes in the range 10^{-5} to 10^{-3} M Zn^{2+}.

its metallic form becomes clear. Both the Pt and Au MEs present variations in the current-potential curves denoted by higher currents for increasing Zn^{2+} concentration but not proportionally to the magnitude change in the Zn^{2+} concentration, Fig. 5b and c. In Fig. 5d the current values selected at the potential of −1.6 V for B-NCD and Au and −1.4 V for Pt, are plotted as a function of the Zn^{2+} concentration evidencing the higher sensitivity of the B-NCD ME in this concentration range.

A more complete study was performed by cycling the B-NCD ME from −0.5 V to −1.8 V in $ZnCl_2$ solutions with varying concentration (10^{-2}, 10^{-3}, 10^{-4}, 10^{-5} and 10^{-6} M) in a 5 mM NaCl background as shown in Fig. 6. The main reactions expected to take place in this range of potentials are the reduction of dissolved oxygen, the reduction of water with hydrogen evolution, the reduction of Zn^{2+} to Zn(s) and the oxidation of Zn(s) back to Zn^{2+} (the waves attributed to each reaction are identified in Fig. 6).

A two-step reaction, $Zn \rightarrow Zn^{+} + e^{-}$ and $Zn^{+} \rightarrow Zn^{2+} + e^{-}$, has been proposed for the zinc dissolution in acidic conditions [46,47], whereas the deposition of zinc in $ZnCl_2$ solution was found to be the reverse of the same two-step reaction [48]. According to Cachet and Wiart [49], the Zn^{+}_{ads} intermediate has an inhibitor effect on hydrogen evolution. In fact, the cathodic reactions on zinc near the zinc reversible potential are dominated by zinc deposition when the zinc concentration is higher than 10^{-4} M [50].

In Fig. 6, the voltammograms for Zn^{2+} concentrations of 10^{-2} M and 10^{-3} M are different from those at lower concentrations. At 10^{-2} M, the polarization towards more negative potentials presents a well-defined plateau of diffusion controlled oxygen reduction until ~−1.25 V, followed by two rising slopes and the corresponding plateaus, one around −1.4 V and the other around −1.6 V, both considered to be related to the deposition of zinc. Excursion towards more negative potentials leads to water reduction with hydrogen evolution, starting around −1.74 V. This potential for H_2 evolution is the most negative of all Zn^{2+} concentrations tested, proving the inhibiting effect of higher concentration of Zn^{2+} on the evolution of this gas. On the reverse sweep, Zn^{2+} continues to deposit up to −1.1 V, then the dissolution of the deposited zinc starts and a marked oxidation peak is observed at approximately −0.9 V. The shape of the voltammogram for 10^{-3} M is similar, except for the absence of the second plateau in the cathodic sweep in the zinc deposition region and for the water reduction which starts earlier. This is probably due to the lower concentration of Zn^{2+}, which makes hydrogen evolution more favorable. No clear plateaus are detected in the cathodic sweep at 10^{-4} M, marking a transition in the behavior of the ME, which is in agreement with reference [50]. On the reverse sweep, diffusion-controlled reduction of Zn^{2+} still occurs, but the oxidation peak intensity is much lower. For 10^{-5} M the reduction of Zn^{2+} at the reverse sweep continues to be measurable but is kinetically controlled with clear dominion of water reduction. At 10^{-6} M the reduction of Zn^{2+} is hardly detectable, as well as the dissolution peak. Conversely, the hydrogen evolution potential for the 10^{-6} M solution is the lowest of all measured concentrations, indicating that it is more favorable at lower zinc concentrations, which is again in good agreement with the previously referred works.

The average background subtracted current values of three reverse sweeps at −1.6 V were plotted against $ZnCl_2$ concentration (Fig. 7). The current–concentration dependence exhibits a linear behavior from 10^{-5} M to 10^{-2} M. The curve for a potential of −1.3 V is also plotted to confirm that the current–concentration linear behavior exists at potentials closer to the potential at which Zn^{2+} reduction starts. This linearity is the principal requirement for the amperometric detection of Zn^{2+}. The detection limit was determined by taking three times the standard deviation for each plot, which sets a value of 7.34×10^{-6} M for the lowest detectable concentration for MEs produced using the conditions given in Section 2 for S3 B-NCD coatings.

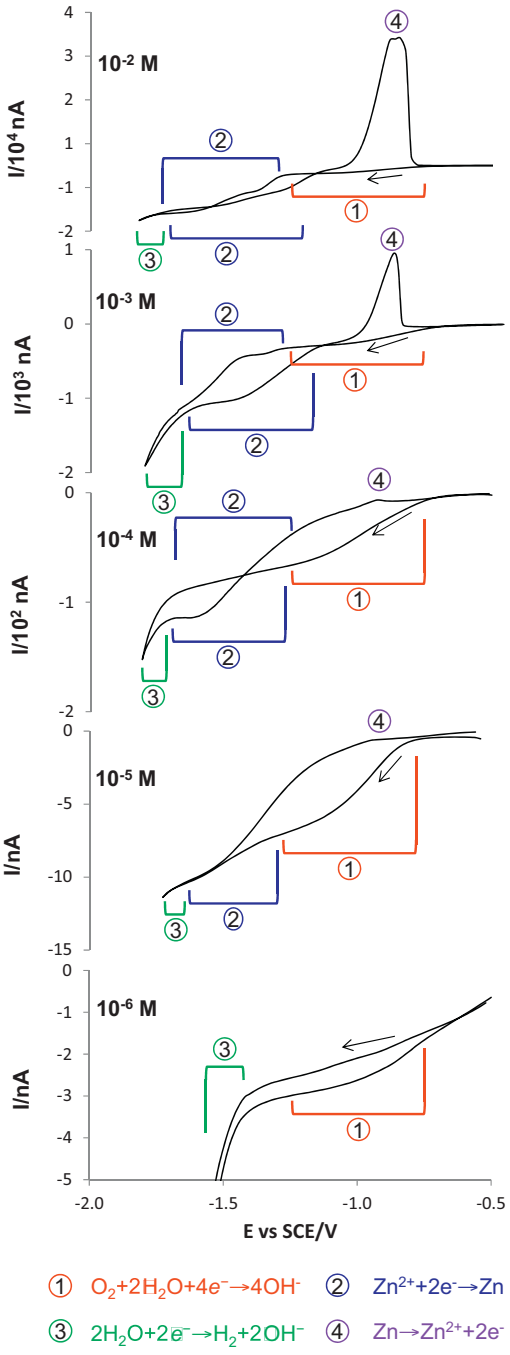

Fig. 6. Voltammograms of a S3 B-NCD microelectrode in $ZnCl_2$ solutions of 10^{-6}, 10^{-5}, 10^{-4}, 10^{-3} and 10^{-2} M in 5 mM NaCl, showing dissolved oxygen reduction (red line), Zn^{2+} reduction (blue line), water reduction (green line) and Zn oxidation. (Note the 10 fold change in the current scale for the different concentrations.) (For interpretation of the references to color in this figure legend, the reader is referred to the web version of this article.)

3.3. Application to the corrosion of a Fe–Zn galvanic couple

In order to evaluate applicability of the B-NCD MEs in investigation of corrosion processes, measurements were performed on a model Fe–Zn galvanic couple immersed in a 5 mM NaCl solution. Fig. 8a depicts a schematic of the cell used and Fig. 8b a representation of the measurements performed over the couple. Fig. 9 shows

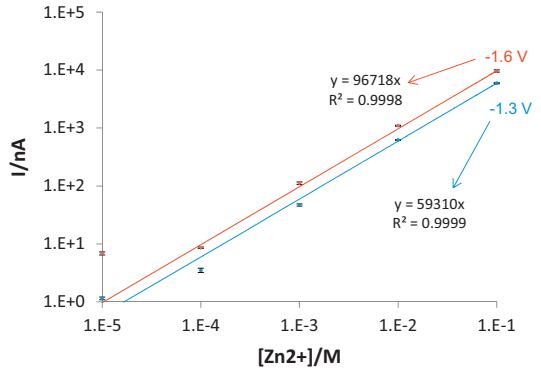

Fig. 7. Relationship between concentration of Zn^{2+} and the reduction current measured by the S3 B-NCD ME at −1.6 and −1.3 V vs SCE from 10^{-6} to 10^{-2} M Zn^{2+}.

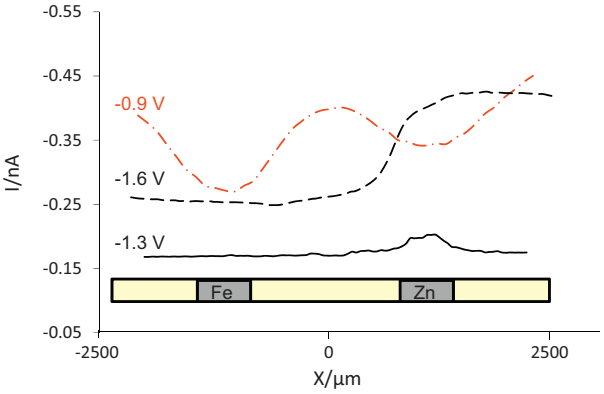

Fig. 9. Linear microamperometric measurements using a S3 ME for Zn^{2+} reduction at −1.6 V (dashed black line) and −1.3 V (continuous black line) and dissolved O_2 reduction at −0.9 V (red dotted line). (For interpretation of the references to color in this figure legend, the reader is referred to the web version of this article.)

the currents related to the reduction of dissolved O_2 or reduction of Zn^{2+} to Zn at the ME, recorded in a line that passed 100 µm above the Fe and Zn electrodes.

The current due to reduction of O_2 was measured with the tip polarized at −0.9 V vs Ag/AgCl and was proportional to the O_2 local concentration. The lowest values where recorded above the iron electrode which is the cathode in the galvanic couple. The oxygen consumption at the Fe surface diminishes its local amount, leaving less to react at the microelectrode tip. The oxygen reduction current also decreases above the zinc anode because, in spite of being it the couple's anode, oxygen reduction also takes place there. This happens since in parallel to the galvanic corrosion there is self-corrosion of zinc which leads to presence of local cathodic areas with oxygen reduction processes on Zn surface.

The oxidation of zinc generates Zn^{2+} ions that can be detected with the microprobe polarized at −1.6 V vs Ag/AgCl. The current raised above the zinc anode as expected but did not return to the values found at the bulk, possibly due to accumulation of metallic zinc at the surface of the ME, with consequent increase in the electroactive area. This accumulation of Zn was found to be the main limitation of the B-NCD ME. Thereby, the test was repeated with a lower applied potential of −1.3 V. In this case, the current increased above the zinc anode only, while a lower constant value was observed for the bulk solution.

The increase of electroactive area by zinc accumulation is confirmed in Fig. 10, where a sequence of cycles between −1.1 and −2.1 V presents a current rise from cycle to cycle, indicating a progressive deposition of this metal at the surface of the ME. If the upper limit of the cycles was −0.8 V instead of −1.1 V, thus including the zinc oxidation, the regeneration of the original surface would take place. Fig. 11 shows a sequence of ten cycles from −0.8 to −1.75 V where the oxidation of the zinc just deposited renews the surface leading to similar voltammograms in every cycle. This can be a solution to overcome the unwanted increase in electrode's area.

The mapping of the concentration of oxygen and zinc ions was also performed using the developed MEs. A potential of −0.9 V was

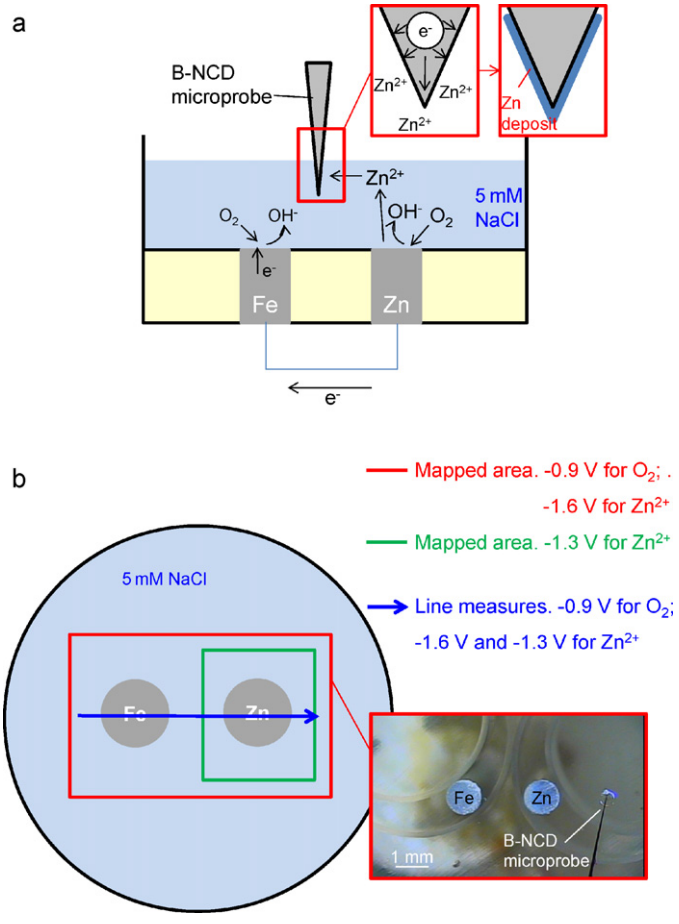

Fig. 8. Experimental setup for microamperometric measurements with a S3 ME. (a) Fe–Zn galvanic couple immersed in 5 mM NaCl for Zn^{2+} and dissolved oxygen detection. (b) Schematics of the measurements performed.

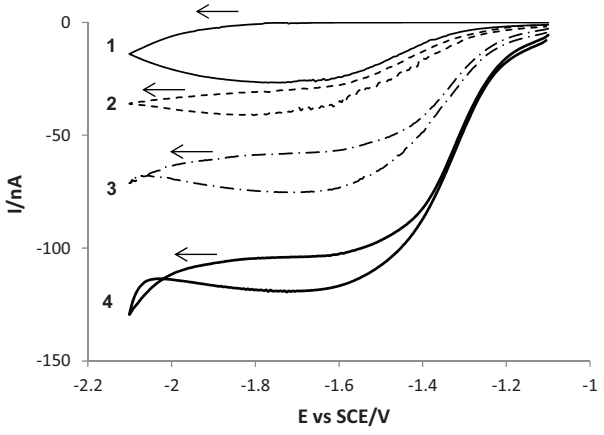

Fig. 10. Voltammograms of the S3 ME cycled from −1.1 to −2.1 V repeatedly, showing a progressive current increase due to accumulation of Zn on the surface of the ME.

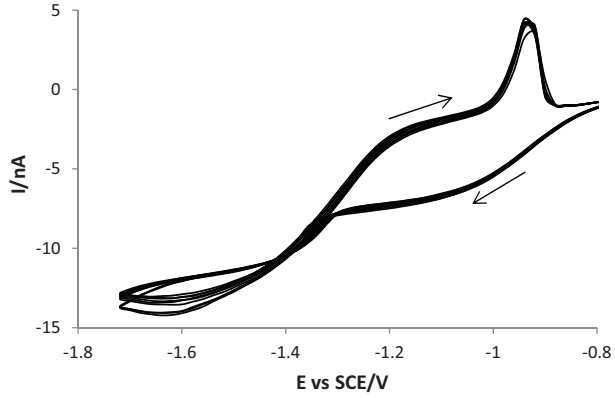

Fig. 11. Voltammograms of the S3 ME during ten consecutive cycles from −0.8 to −1.75 V, showing the reproducibility of the measurements if the B-NCD surface is renewed by Zn oxidation to the bulk.

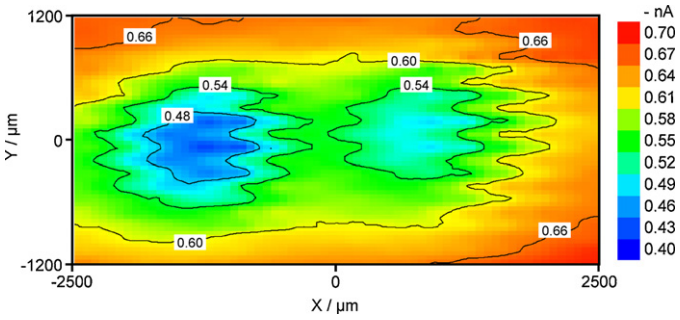

Fig. 12. Map of dissolved oxygen detected microamperometrically with a S3 ME polarized at −0.9 V vs. Ag/AgCl.

applied for mapping the distribution of dissolved oxygen, 100 µm above the entire area of the galvanic couple (Fig. 12). As observed for the line measurements, the current was lower above the metallic regions (lowest above Fe), keeping a constant higher value in the bulk solution surrounding the galvanic couple. A potential of −1.3 V was applied to the tip in order to map the distribution of Zn^{2+} in the same area as for oxygen. The result presented a current increase in the beginning, after which the ME lost the sensibility, showing a nearly invariable current for all the remaining area. This may have been caused by zinc accumulation and surface blocking due to zinc oxide or zinc hydroxide formation, since the local pH above the iron cathode is expected to be considerably higher than in the rest of the NaCl solution, as OH^- is the product of the reduction of dissolved oxygen. Conversely, by mapping only above the zinc anode (Fig. 13), a current raise was observed above the anodic region, what seems to support the surface blocking hypothesis for the mapping of the full Zn–Fe couple area. Solutions for this problem may outcome from further exploring the growth conditions or surface functionalization of the CVD diamond films.

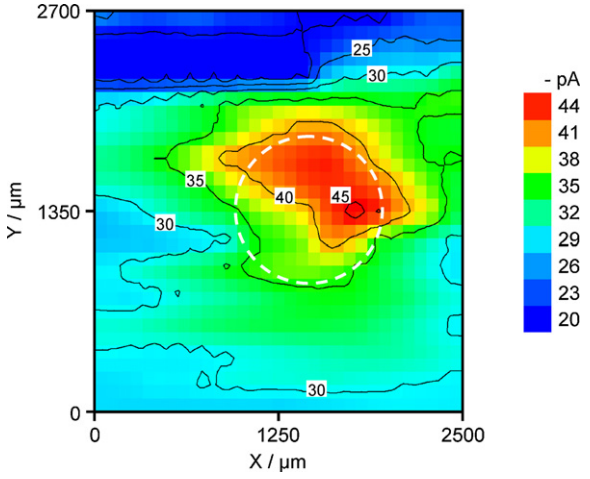

Fig. 13. Map of Zn^{2+} detected microamperometrically with a S3 ME polarized at −1.3 V vs Ag/AgCl (the dashed circle indicates the position of the zinc electrode).

4. Conclusions

Boron doped nanocrystalline diamond microelectrodes were produced and tested towards their prospective use in corrosion studies. The electrodes showed a wide working potential window (~3.5 V) and low background current in 5 mM NaCl, which was the medium intended for the corrosion testing. Good electrochemical reversibility was confirmed with the $Fe(CN)_6^{3-/4-}$ redox system. A linear relationship was found between the zinc reduction current and Zn^{2+} concentrations from 10^{-5} M to 10^{-2} M in a 5 mM NaCl background solution. The microelectrodes were tested as amperometric microprobes to map the oxygen and Zn^{2+} distribution in solution above a Fe-Zn galvanic couple. It was possible to detect, with lateral resolution, the decrease of O_2 near both metals and zinc cations production at the anode. Although B-NCD MEs have shown the capability to detect Zn^{2+}, further optimization is still required to avoid a significant deposition of metallic zinc, which was the main drawback observed.

Acknowledgments

E.L. Silva, A.C. Bastos and M.A. Neto would like to acknowledge FCT (Fundação para a Ciência e a Tecnologia) for the grants SFRH/BD/61675/2009, SFRH/BPD/23175/2005 and SFRH/BPD/45610/2008, respectively. This work was supported by project PTDC/CTM-MET/113645/2009, funded by FEDER through COMPETE programmme-Operacional Factors for Competitivity and by national funds through FCT – Portuguese Science and Technology Foundation.

References

[1] M. Amaral, E. Salgueiredo, F.J. Oliveira, A.J.S. Fernandes, F.M. Costa, R.F. Silva, Surface and Coatings Technology 200 (2006) 6409.
[2] Y.V. Pleskov, A.Y. Sakharova, M.D. Krotova, L.L. Bouilov, B.V. Spitsyn, Journal of Electroanalytical Chemistry 19 (1987) 228.
[3] P. May, W. Ludlow, M. Hannaway, P. Heard, J. Smith, K. Rosser, Diamond and Related Materials 17 (2008) 105.
[4] C. Wang, A. Hatta, N. Jiang, J. Won, T. Ito, Thin Solid Films 308–309 (1997) 279.
[5] A. Manivannan, D.A. Tryk, A. Fujishima, Diamond Electrochemistry, 1st ed., Elsevier Science, 2005, pp. 342–374.
[6] S. Basu, W.P. Kang, J.L. Davidson, B.K. Choi, A.B. Bonds, D.E. Cliffel, Diamond and Related Materials 15 (2006) 269.
[7] A. Suzuki, T. Ivandini, K. Yoshimi, A. Fujishima, G. Oyama, T. Nakazato, N. Hattori, S. Kitazawa, Y. Einaga, Analytical Chemistry 79 (2007) 8608.
[8] A. Kraft, International Journal of Electrochemical Science 2 (2007) 355.
[9] J.B. Cooper, S. Pang, S. Albin, J. Zheng, R.M. Johnson, Analytical Chemistry 70 (1998) 464.
[10] A.J. Bard, L.R. Faulkner, Electrochemical Methods, Marcel Dekker Inc, New York, 2001, p. 165.
[11] E.L. Silva, M.A. Neto, A.J.S. Fernandes, A.C. Bastos, R.F. Silva, M.L. Zheludkevich, F.J. Oliveira, Diamond and Related Materials 19 (2010) 1330.
[12] Y. Zhoua, J. Zhia, Talanta 79 (2009) 1189.
[13] J. Zhao, J. Wang, J. Zhi, Z. Zhang, Science China Chemistry 53 (2010) 1378.
[14] J. Park, V. Quaiserova-Mocko, B.A. Patel, M. Novotny, A. Liu, X. Bian, J.J. Galligan, G.M. Swain, Analyst 133 (2008) 17.
[15] P. Siew, K. Loh, W. Poh, H. Zhang, Diamond and Related Materials 14 (2005) 426.
[16] K. Soh, W. Kang, J. Davidson, Y. Wong, D. Cliffel, G. Swain, Diamond and Related Materials 17 (2008) 900.
[17] C.A. Martínez-Huitle, Small 3 (2007) 1474.
[18] Z. Chomisteková, J. Sochr, J. Svítková, L. Švorc, Acta Chimica Slovenica 4 (2011) 11.

[19] N.Y. Stozhko, N.A. Malakhova, M.V. Fyodorov, K.Z. Brainina, Journal of Solid State Electrochemistry 12 (2007) 1219.
[20] A. Avdic, A. Lugstein, M. Wu, B. Gollas, I. Pobelov, T. Wandlowski, K. Leonhardt, G. Denuault, E. Bertagnolli, Nanotechnology 22 (2011) 145306.
[21] A.C. Bastos, O.V. Karavai, M.L. Zheludkevich, K.A. Yasakau, M.G.S. Ferreira, Electroanalysis 22 (2010) 2009.
[22] A.M. Simoes, A.C. Bastos, M.G. Ferreira, Y. González-García, S. Gonzalez, R.M. Souto, Corrosion Science 49 (2007) 726.
[23] J. Rogalska, M.M. Brzóska, A. Roszczenko, J. Moniuszko-Jakoniuk, Chemico-Biological Interactions 177 (2009) 142.
[24] L.C. Costello, R.B. Franklin, P. Feng, Mitochondrion 5 (2005) 143.
[25] Z. Luo, X. Tan, J. Zheng, Q. Chen, C. Liu, Aquaculture 319 (2011) 150.
[26] B. Szewczyk, M. Sowa, A. Czupryn, J.M. Wierońska, P. Brański, K. Sadlik, W. Opoka, W. Piekoszewski, M. Smiałowska, J. Skangiel-Kramska, A. Pilc, G. Nowak, Brain Research 1090 (2006) 69.
[27] Y. You, E. Tomat, K. Hwang, T. Atanasijevic, W. Nam, A.P. Jasanoff, S.J. Lippard, Chemical Communications 46 (2010) 4139.
[28] S. Yilmaz, S. Yagmur, G. Saglikoglu, M. Sadikoglu, International Journal of Electrochemical Science 4 (2009) 288.
[29] K. Strasunske, Ø. Mikkelsen, G. Billon, Electroanalysis 22 (2010) 501.
[30] E. Tada, S. Satoh, H. Kaneko, Electrochimica Acta 49 (2004) 2279.
[31] A.C. Bastos, M.G. Taryba, O.V. Karavai, M.L. Zheludkevich, S.V. Lamaka, M.G.S. Ferreira, Electrochemistry Communications 12 (2010) 394.
[32] V.K. Gupta, R.N. Goyal, M. Khayat, P. Kumar, N. Bachheti, Talanta 69 (2006) 1149.
[33] E. McGaw, G.M. Swain, Analytica Chimica Acta 575 (2006) 180.
[34] P. Sonthalia, E. Mcgaw, Y. Show, G.M. Swain, Analytica Chimica Acta 522 (2004) 35.
[35] S. Prawer, R.J. Nemanich, Philosophical Transactions A 362 (2004) 2537.
[36] M. Anik, Corrosion Science 48 (2006) 4158.
[37] A.F. Azevedo, M.R. Baldan, N.G. Ferreira, International Journal of Electrochemistry 2012 (2012) 1.
[38] D. Das, R.N. Singh, International Materials Reviews 52 (2007) 29.
[39] J.H. Luong, K.B. Male, J.D. Glennon, Analyst 134 (2009) 1965.
[40] I. Duo, A. Fujishima, C. Comninellis, Journal of Applied Electrochemistry 34 (2004) 935.
[41] T.N. Rao, A. Fujishima, Diamond and Related Materials 9 (2000) 384.
[42] J.P. Goss, R.J. Eyre, P.R. Briddon, Physica Status Solidi B 245 (2008) 1679.
[43] P. Monk, Electroanalytical Chemistry, John Wiley & Sons, 2001, p. 158.
[44] M. Pourbaix, Atlas of Electrochemical Equilibria in Aqueous Solutions, 2nd ed., National Association of Corrosion Engineers, 1974.
[45] E. Tada, K. Sugawara, H. Kaneko, Electrochimica Acta 49 (2004) 1019.
[46] L.M. Baugh, Electrochimica Acta 24 (1979) 657.
[47] T. Hurlen, K.P. Fischer, Journal of Electroanalytical Chemistry and Interfacial Electrochemistry 61 (1975) 165.
[48] J.T. Kim, J. Jorné, Journal of the Electrochemical Society 127 (1980) 8.
[49] C. Cachet, R. Wiart, Journal of Applied Electrochemistry 20 (1990) 1009.
[50] X.G. Zhang, Corrosion and Electrochemistry of Zinc, Plenum Press, 1996, p. 36.